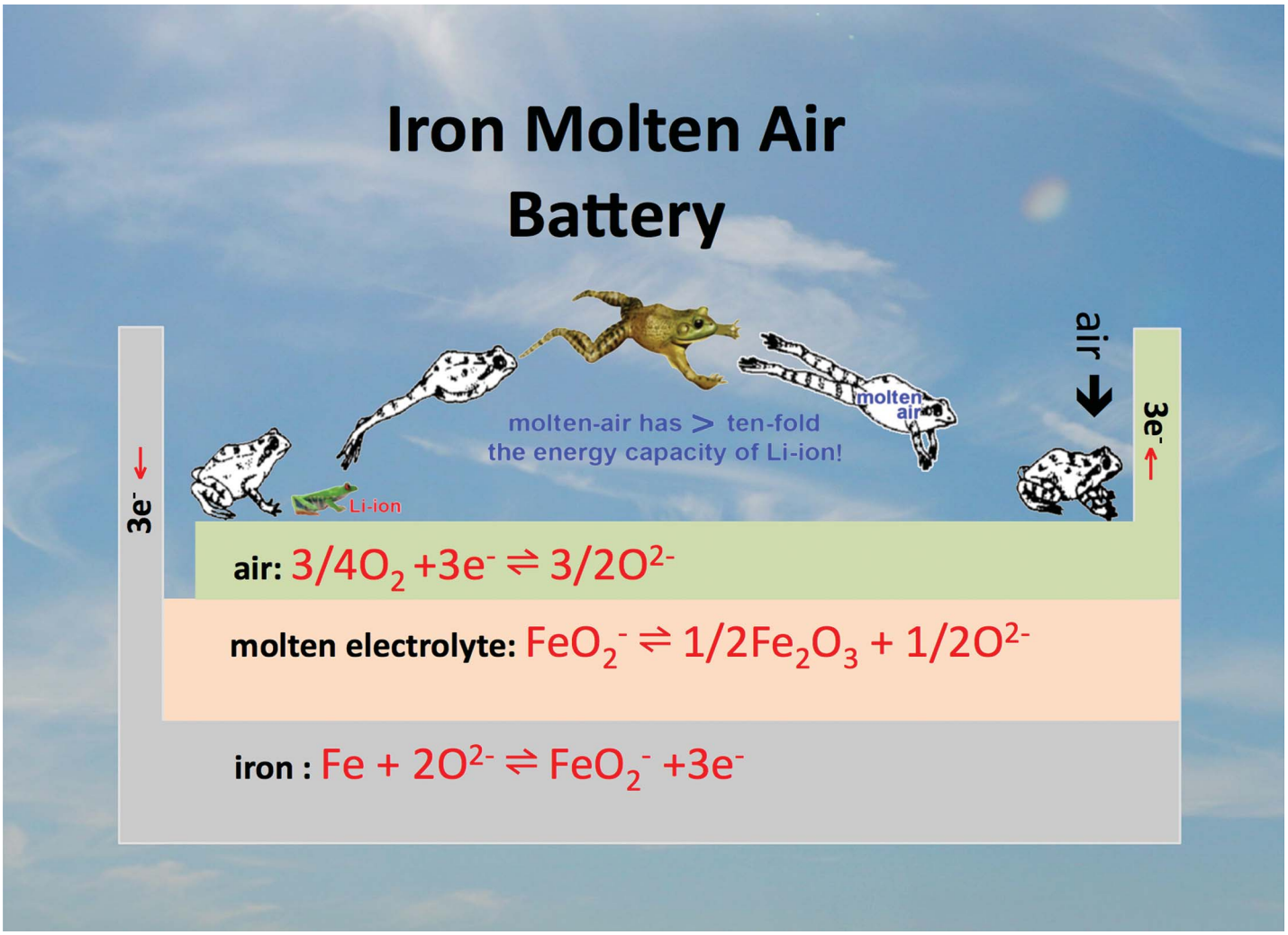

Showcasing collaborative research from the Northeast Petroleum University (Daqing, China) and the George Washington University (Washington, DC).

A long cycle life, high coulombic efficiency iron molten air battery

Molten air batteries, such as the iron molten air battery, that use a molten electrolyte are rechargeable, and have amongst the highest intrinsic battery storage capacities. This research studies advances in molten air batteries, enhancing their long cycle life and safety with a new interfacial higher-activity air electrode and a low operating temperature molten eutectic carbonate electrolyte.

As featured in:

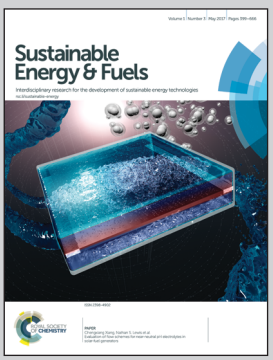

See Shuzhi Liu, Stuart Licht *et al.*, *Sustainable Energy Fuels*, 2017, **1**, 474.

ROYAL SOCIETY OF CHEMISTRY

rsc.li/sustainable-energy

Registered charity number: 207890

Sustainable Energy & Fuels

PAPER

Cite this: *Sustainable Energy Fuels*, 2017, **1**, 474

A long cycle life, high coulombic efficiency iron molten air battery

Baochen Cui,[ab] Wei Xiang,[ab] Shuzhi Liu,*[ab] Hongyu Xin,[ab] Xianjun Liu[ab] and Stuart Licht*[c]

Received 1st December 2016
Accepted 7th March 2017

DOI: 10.1039/c6se00082g

rsc.li/sustainable-energy

Despite the recent advancements in iron molten air batteries, great challenges still remain to realize cycling stability, high energy efficiency and a long-term cycling life. Herein, we demonstrate a new iron molten air battery for large-scale energy storage. We replace the KCl–LiCl–LiOH eutectic electrolyte used in our previous study with a $Li_{0.87}Na_{0.63}K_{0.50}CO_3$ eutectic electrolyte with added NaOH and LiOH. A fin air electrode configuration is designed to improve the coulombic efficiency. Cycling tests for the iron molten air battery showed a stable performance through 450 cycles with nearly 100% coulombic efficiency and an average discharge potential of ~1.08 V when charged at a constant current of 0.05 A and discharged over a constant 100 Ω load to a 0.7 V cutoff at 500 °C. Moreover, the iron molten air battery had an excellent high-rate response up to 6.4C with a high coulombic efficiency of 95.1%. These results provide critical advances in developing iron molten air batteries with high efficiency and a long-term service life.

Introduction

With the growing demand for large-scale power generating systems that can incorporate utilization of intermittent renewable energy sources from the sun and the wind, rechargeable metal–air batteries have long been recognized as one of the most promising candidates for grid storage.[1,2] These metal–air batteries feature an open cell structure, which admits the supply of the cathode discharge active material (oxygen) continuously and abundantly from an external source (air). Due to the fact that the cathodic oxygen is from air and not stored in the cell, the metal–air family has a notably higher theoretical energy density, compared with other traditional batteries such as primary Zn–MnO_2 (Zn–Mn), rechargeable lead–acid, nickel–metal hydride (Ni–MH), flow redox cells and sodium–sulphur batteries and the currently commercialized Li-ion batteries.[3,4]

Among metal–air batteries, iron–air batteries have been studied in recent years. Fe is the fourth most common element in the earth's crust,[5] next to aluminum, oxygen, and silicon. Fe is a low cost metal whose theoretical specific energy density based on the 3-electron oxidation of iron, 1440 A h kg^{-1}, is high.[6] Additionally, Fe is much safer to use and handle than Li, and its compounds are non-toxic and environmentally benign. It has been reported that the iron electrode, one of the most robust electrodes known to battery electrochemists, can withstand over 3000 cycles with no significant degradation in nickel–iron batteries; unlike zinc electrodes, the iron electrode does not suffer from shape change upon cycling and is also extremely tolerant to overcharge and over-discharge.[7] By virtue of its various advantages, Fe is a natural candidate as an anode discharge material in high-energy-density battery systems.

Conventional iron–air batteries normally consist of one iron electrode with two air-breathing electrodes, one on each side, in a plane parallel configuration, using an aqueous alkaline electrolyte such as KOH.[8] However, in an aqueous alkaline electrolyte, the use of iron anodes suffers from a number of problems including parasitic hydrogen evolution and passivation. One direction has been to improve these anodes by using carbon materials as electrode additives.[9–11] It is also found that hydrogen evolution was inhibited by additives such as Bi_2S_3, Bi_2O_3, FeS, Na_2S and K_2S in the electrode or in the electrolyte.[12–17] However, although many methods have been investigated, it has been established that it is impossible to prevent hydrogen evolution completely.[4]

Recently, Tsuneishi and co-workers have reported a new iron–air secondary battery using KOH–LDH (Mg–Al layered double hydroxide) as a solid electrolyte, but the battery exhibited only about a stable 30% charge–discharge efficiency at room temperature.[18] Another type of solid electrolyte iron–air battery based on reversible solid oxide fuel cells (RSOFCs) and a redox-couple (H_2/H_2O-mediated FeO/Fe) energy storage unit was reported.[19,20] However, the redox cycle stability due to reoxidation and aggregation of the anode at a high temperature is a common issue that needs to be overcome.[21]

[a]*College of Chemistry and Chemical Engineering, Northeast Petroleum University, Daqing 163318, China. E-mail: lszcbccx@163.com; Tel: +86 459 6504758*

[b]*Province Key Laboratory of Oil and Natural Gas Chemical Industry, Northeast Petroleum University, Daqing 163318, China*

[c]*Department of Chemistry, George Washington University, Washington, DC, 20052, USA. E-mail: slicht@gwu.edu; Tel: +1 202 994 6121*

We introduced a new class of rechargeable batteries, the molten (electrolyte) air batteries, in 2013, and used Li_2CO_3 as the electrolyte, and a nickel crucible as an air electrode. The iron molten air battery at 730 °C exhibited a coulombic efficiency of 75% and a voltage efficiency of 84% to a discharge cut-off voltage of 0.8 V.[6] In 2014, we replaced Li_2CO_3 with a lower melting carbonate eutectic ($Li_{0.87}Na_{0.63}K_{0.50}CO_3$ eutectic that melts at 393 °C). At 600 °C, the iron molten air battery exhibits reversible cycling at a 60% coulombic efficiency to a 0.8 V voltage cut-off with a constant current average charge at 1.3 V and a constant load (200 Ω) average discharge of 1.0 V.[22] Recently, we have used the KCl–LiCl–LiOH eutectic with added NaOH as an alternative electrolyte. The battery was cycled at 500 °C for 60 cycles with the highest coulombic efficiency of 66.7%, but decreased to 55.1% in the 60th cycle.[23]

Despite this progress in iron molten air batteries, there are still challenges hindering their commercial applications, including sluggish kinetics, low coulombic efficiency and a short cycle life. In this paper, our research is directed toward the simultaneous optimization of electrolyte formulation together with the electrode architecture to improve the battery performance. The result is an iron molten air battery with a cycle lifespan extended to more than 450 cycles with nearly 100% coulombic efficiency. This work provides critical advances in developing iron molten air batteries with high efficiency and a long-term service life.

Experimental

Materials and methods

Chemicals and materials utilized are lithium carbonate (Li_2CO_3, 97%), sodium carbonate (Na_2CO_3, anhydrous, 99.8%), potassium carbonate (K_2CO_3, anhydrous, 99.0%), lithium hydroxide (LiOH, anhydrous, 95 wt%), sodium hydroxide (NaOH, 96%) and ferric oxide (Fe_2O_3, 99.5%) which are combined to form various molten eutectic electrolytes (x mol% $Li_{0.87}Na_{0.63}K_{0.50}CO_3$ eutectic–y mol% LiOH) with Fe_2O_3 and NaOH. A 2 mm pure Ni wire (99.5%), pure Ni foil (99.95%), 1.2 mm Fe wire (annealed), steel foil (316 steel), and pure alumina (99.7%) crucible are used to make electrodes and are combined to form various cell configurations. Nickel materials are shown to be highly effective for the reversible oxygen electrode and iron materials for the reversible iron electrode of iron molten air batteries.

Cyclic voltammetry (CV) measurements of the iron molten air battery were recorded in the voltage window ranging from −1.50 to 0 V at sweep rates of 50, 100, 150, and 300 mV s^{-1} at 500 °C on an electrochemical workstation (CS350, Wuhan CorrTest instruments Co. Ltd., China). The electrolyte consists of 56.5 mol% $Li_{0.87}Na_{0.63}K_{0.50}CO_3$ eutectic–43.5 mol% LiOH with 0.5 m (m = molal, moles per kilogram of the electrolyte) Fe_2O_3 and 3 m NaOH. A steel foil (2 cm × 2.5 cm) was used as the working electrode. A nickel foil (2 cm × 2.5 cm) was used as the counter and the reference electrode. Electrochemical impedance spectroscopy (EIS) was performed to characterize the conductivity of the mixed electrolyte by measuring the resistance on an electrochemical workstation (CS350, Wuhan CorrTest instruments Co. Ltd., China). A nickel foil (1 cm × 1 cm) was used as the working electrode. A steel foil (1 cm × 1 cm) was used as the counter and the reference electrode located at a distance of 1 cm from the nickel foil. The frequency range used was from 10 mHz to 100 kHz, starting from a high frequency to a low frequency in a logarithmic scan. The alternating voltage amplitude was set to 10 mV. XRD patterns were compared with PDF data of MDI Jade 5.0 to identify the phases of each sample by powder X-ray diffraction with a Cu Kα source (Rigaku D/MAX-2200). Each sample was scanned from 2θ of 10 to 80°. Field-emission scanning electron microscopy (FE-SEM, Zeiss Sigma) was employed to characterize the surface morphology of the air electrode. The electrode samples were prepared by gold sputtering treatment.

The cell is situated within an 1800 W band heater, and insulated by rigid thermal shock resistant ceramic insulation without a binder. Temperature is monitored using a thermocouple and controlled using a temperature controller (708P, YUDIAN automation technology Co. Ltd., China). The charge–discharge behaviors were studied on a LANHE battery testing system (CT2001A, Wuhan LAND electronics Co. Ltd, China) at 500 °C.

Calculations

Thermodynamic electrolysis potentials for iron oxide reduction are calculated from the unit activity thermochemical data of the individual species, using the negative potential necessary to drive a non-spontaneous potential from the reactions: $\sum_{i=1\ \text{to}\ x} r_i R_i \rightarrow \sum_{i=1\ \text{to}\ y} c_i C_i$ using eqn (1)–(5):

$$E^\circ(T) = -\Delta G^\circ(T)/nF \quad (1)$$

$$\Delta G^\circ(T) = \sum_{i=1\ \text{to}\ y} c_i G^\circ(C_i, T) - \sum_{i=1\ \text{to}\ x} r_i G^\circ(R_i, T) \quad (2)$$

$$G^\circ(T) = H^\circ(T) - TS^\circ(T) \quad (3)$$

$$H^\circ(T) - H^\circ_{298.15} = A \times t + B \times t^2/2 + C \times t^3/3 + D \times t^4/4 - E/t + F - H \quad (4)$$

$$S^\circ(T) = A\ \ln(t) + B \times t + C \times t^2/2 + D \times t^3/3 - E/(2 \times t^2) + G \quad (5)$$

where, $E^\circ(T)$ is the electrolytic potential at T (V). T is the temperature (K). n is the number of redox electrons transferred in the reaction. F is the Faraday constant (96 485 C mol^{-1}). $\Delta G^\circ(T)$ is the standard Gibbs free energy change at T (kJ mol^{-1}). $G^\circ(T)$ is the standard Gibbs free energy at T (kJ mol^{-1}). $H^\circ(T)$ is the standard enthalpy at T (kJ mol^{-1}). $S^\circ(T)$ is the standard entropy at T (J mol^{-1} K^{-1}). t is the temperature as, T (K)/1000. A through G are thermodynamic Shomate parameters from the NIST chemistry WebBook.

Results and discussion

Formation of the electrolyte

The electrolyte system is crucial for the battery, and affects electrochemical activity, corrosion, electrolyte loss rate and so

on. The molten salt electrolyte provides a number of advantages over the common aqueous alkaline electrolyte. With a wide electrochemical window, the molten salt electrolyte is electrochemically stable, avoiding the common aqueous alkaline electrolyte issue of hydrogen evolution (decomposition of water to H_2 and O_2).[24] The thermal stability and low vapor pressure of the molten salt electrolyte avoid "drying out of the electrolyte," which is problematic in aqueous air batteries. Additionally, a benefit associated with this high temperature cell is that noble metal catalysts are not required for the cell electrochemical oxidation and reduction processes.[25] One of the disadvantages is the requirement for electrolyte management, which is necessary to find solutions to some of the electrolyte loss issues by electrolyte migration and electrolyte vaporization, and we note that molten carbonate fuel cells (MCFCs) have exhibited a similar experience.[25,26] 11.5 mol% KCl–45 mol% LiCl–43.5 mol% LiOH eutectic containing NaOH was used for the iron molten air battery in our previous study.[23] However, chloride salts exhibit relatively poor solubility for the O^{2-} ion,[27] and are thus not expected to be used in the iron molten air battery. In addition, the iron molten air battery with the $Li_{0.87}Na_{0.63}K_{0.50}CO_3$ eutectic containing Li_2O exhibited high polarization and low coulombic efficiency at 500 °C over a 100 Ω load. The melting point of the $Li_{0.87}Na_{0.63}K_{0.50}CO_3$ eutectic is 393 °C, lower than 500 °C. Here, we replace the chloride salts (KCl–LiCl) in the 11.5 mol% KCl–45 mol% LiCl–43.5 mol% LiOH eutectic with a $Li_{0.87}Na_{0.63}K_{0.50}CO_3$ eutectic to improve the performances of the iron molten air battery. Fig. 1 and 2 present the charge–discharge cycling of the iron molten air battery in a $Li_{0.87}Na_{0.63}K_{0.50}CO_3$ eutectic electrolyte containing 3 m NaOH and 0.5 m Fe_2O_3 without or with LiOH at 500 °C. As shown in Fig. 1, the iron molten air battery with the $Li_{0.87}Na_{0.63}K_{0.50}CO_3$ eutectic (without LiOH) exhibits a significant loss in discharge compared to the charging potential, and almost no discharge voltage plateau is observed. As observed in Fig. 2, and as expected, compared to the $Li_{0.87}Na_{0.63}K_{0.50}CO_3$ eutectic without LiOH, the addition of 43.5 mol% LiOH to the $Li_{0.87}Na_{0.63}K_{0.50}CO_3$ eutectic decreases the discharge polarization and improves the coulombic efficiency to around ~77.5%. The melting point of the ternary LiNaK carbonates can be further decreased from the minimum alkali eutectic carbonate melting point of 399 °C by about 50 °C to ~340 °C with the addition of an alkali hydroxide.[28] The low melting point leads to a decrease of viscosity to promote mass transfer, especially, make the escaping of oxygen bubbles from the air electrode easier, reducing the charge polarization. Moreover, the addition of an alkali hydroxide helps in the formation of lithium nickel oxide on the nickel air electrode. It is worthy of note that the iron molten air battery containing 56.5 mol% $Li_{0.87}Na_{0.63}K_{0.50}CO_3$

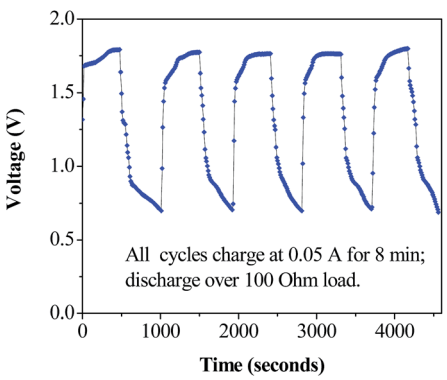

Fig. 1 Cycling characteristics of an iron molten air battery exhibiting large hysteresis without LiOH. The molten $Li_{0.87}Na_{0.63}K_{0.50}CO_3$ electrolyte contains 0.5 m Fe_2O_3 and 3 m NaOH without LiOH. Electrode configuration: the air electrode of cylindrical nickel foil (2 cm height, 20 cm^2) outside the counter electrode of cylindrical steel foil (1 cm height, 4 cm^2). The molten electrolyte is sufficient to cover the steel foil counter electrode. The immersion depth of the air electrode in the molten salt is 1 cm. The battery is cycled by consistent current charging at 0.05 A and constant load discharging over a 100 Ω load to a 0.7 V cutoff at 500 °C.

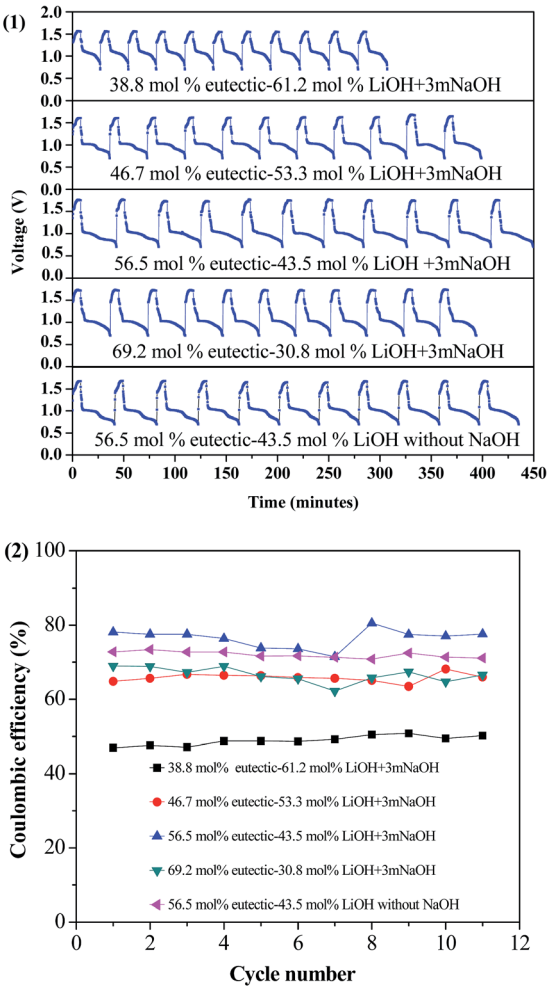

Fig. 2 The effect of electrolyte systems on the charge–discharge behaviour. (1) Cycling characteristics. (2) Coulombic efficiency. Electrode configuration: the air electrode of cylindrical nickel foil (2 cm height, 20 cm^2) outside the counter electrode of cylindrical steel foil (1 cm height, 4 cm^2). The molten electrolyte is sufficient to cover the steel foil counter electrode. The immersion depth of the air electrode in the molten salt is 1 cm. In each of the experiments, each of the eleven cycles is at 0.05 A charge followed by discharge over a 100 Ω load to a 0.7 V cutoff at 500 °C.

eutectic–43.5 mol% LiOH eutectic and 0.5 m Fe_2O_3 but without NaOH exhibited a coulombic efficiency of ~71% at 500 °C, which is lower than that containing 56.5 mol% $Li_{0.87}Na_{0.63}K_{0.50}CO_3$ eutectic–43.5 mol% LiOH eutectic and 0.5 m Fe_2O_3 with 3 m NaOH. Fe_2O_3 reacts with NaOH to form $NaFeO_2$, a crucial intermediate product for deposition–dissolution of iron in the charge/discharge reaction.[22] We further probed the magnitude of the effect of LiOH concentrations on coulombic efficiency. When the LiOH concentration is decreased to 30.8 mol% (69.2 mol% $Li_{0.87}Na_{0.63}K_{0.50}CO_3$ eutectic–30.8 mol% LiOH), the coulombic efficiency of the battery diminishes to ~62.2%. The coulombic efficiencies are respectively lowered to ~63.4 and ~47.0% with increase of LiOH concentrations to 53.3 mol% and 61.2 mol% although the charge polarizations are improved compared to low LiOH concentrations.

In order to probe and understand the ionic conductivity of the mixed electrolyte and the cell resistance of the battery, EIS studies were performed in this work. As shown in Fig. 3(1), while at high frequencies the inductive data can be ascribed to the connection leads to the battery, the intercept with the *x* axis (through imaginary parts, Z'' axis, at 0 Ω) corresponds to the ohmic resistance of the battery cell, including the electrolyte resistance, contact resistances, electronic contact resistances, *etc.* The ohmic resistance results are summarized in Fig. 3(2). It is clear that the ohmic resistance decreases with increase of the LiOH concentration, reaches the lowest value of 1.07 Ω for the 56.5% mol $Li_{0.87}Na_{0.63}K_{0.50}CO_3$ eutectic–43.5% mol LiOH electrolyte with 3 m NaOH, indicating a good conductivity.

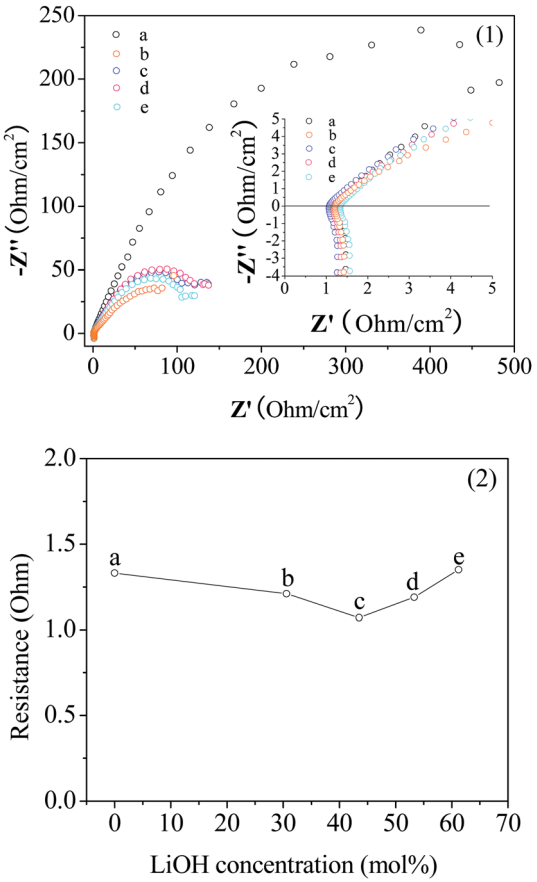

Fig. 3 (1) Nyquist plots of the $Li_{0.87}Na_{0.63}K_{0.50}CO_3$ eutectic with 3 m NaOH without adding LiOH and with adding LiOH. Inset is the close-up of the high-frequency range. The electrolyte systems: $Li_{0.87}Na_{0.63}K_{0.50}CO_3$ eutectic with 3 m NaOH (a) without adding LiOH, (b) with adding 30.8 mol% LiOH, (c) with adding 43.5 mol% LiOH, (d) with adding 53.3 mol% LiOH, and (e) with adding 61.2 mol% LiOH. (2) Ohmic resistances for the mixed electrolytes.

Deposition–dissolution of iron

The deposition–dissolution of iron in 56.5 mol% $Li_{0.87}Na_{0.63}K_{0.50}CO_3$ eutectic–43.5 mol% LiOH with 0.5 m Fe_2O_3 and 3 m NaOH at 500 °C was studied by cyclic voltammetry using a steel foil (2 cm × 2.5 cm) as the working electrode and a nickel foil (2 cm × 2.5 cm) as the counter and the reference electrode at different sweep rates. Voltammetric sweeps during the initial five cycles are shown in Fig. 4. Two cathodic peaks at around −0.49 V (E_{pc1}) and −1.07 V (E_{pc2}) were observed in the first cycle. In order to identify the peaks of voltammograms, we calculated the thermodynamic electrolysis potentials for electrochemical reduction of Fe_2O_3.[29–31] As shown in Fig. 5, with increase of the reduction potential, three reactions for the reduction of Fe_2O_3 may occur in sequence at 500 °C:

$$2Fe_2O_3 \rightleftharpoons 4FeO + O_2 \ (E^0_{Fe(III)/Fe(II)} = -0.46\ V,\ 500\ ^\circ C) \quad (6)$$

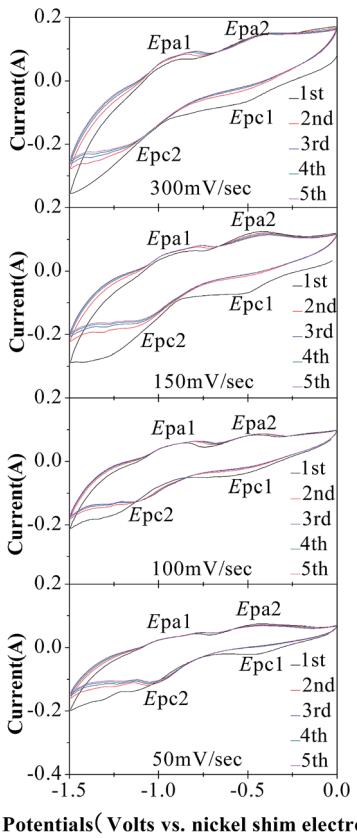

Fig. 4 Cyclic voltammograms of the iron anode in a 56.5 mol% $Li_{0.87}Na_{0.63}K_{0.50}CO_3$ eutectic–43.5 mol% LiOH electrolyte containing 0.5 M Fe_2O_3 and 3 M NaOH at various scan rates at 500 °C.

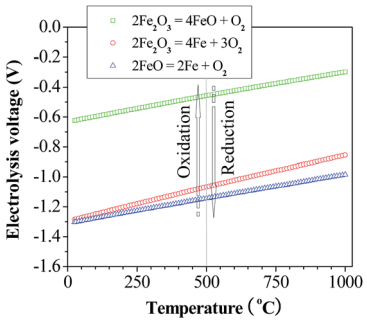

Fig. 5 Thermodynamic electrolysis potentials for electrochemical reduction of Fe_2O_3.

$$2Fe_2O_3 \rightleftharpoons 4Fe + 3O_2 \ (E^0_{Fe(III)/Fe(0)} = -1.07\ V,\ 500\ ^\circ C) \quad (7)$$

$$2FeO \rightleftharpoons 2Fe + O_2 \ (E^0_{Fe(II)/Fe(0)} = -1.14\ V,\ 500\ ^\circ C) \quad (8)$$

Iron metal deposition was performed in this molten electrolyte with addition of 3 m NaOH and 0.5 m Fe_2O_3 using a steel foil (2 cm × 2.5 cm) as the cathode and a nickel foil (2 cm × 2.5 cm) as the anode at 500 °C by charging at a constant current. Fig. 6 compares our experimental measurements of the XRD patterns of the electrolyte, and deposition products on the steel electrode before and after washing with water. Compared to the XRD pattern of the electrolyte, the XRD pattern of the deposition products before washing exhibits new 2-theta peaks at 65.0°, and no FeO peaks suggesting that the FeO produced in eqn (6) was reduced in reaction of eqn (8). It is clear that the peaks of the electrolyte disappear in the XRD pattern of products separated with a magnetic stirrer after washing with water to remove the electrolyte deposition products, whereas, the 2-theta peaks at 65.0° remain unchanged, matching the library XRD of pure iron (MDI Jade 5.0, PDF 06-0696) (Fig. 6). This verified that iron metal was produced during charging.

Consistent with the voltammograms in Fig. 4, we suggest that the observed cathodic peak (E_{pc1}) at approximately −0.49 V is due to the reduction of Fe(III)/Fe(II) (eqn (6)), and the reduction peak (E_{pc2}) at around −1.07 V is attributed to the reduction of Fe(III)/Fe(0) (eqn (7)) and Fe(II)/Fe(0) (eqn (8)). As shown in Fig. 4, with further cycling, two anodic peaks were observed, including one peak at around −0.92 V (E_{pa1}), ascribed to the oxidation of Fe(0)/Fe(II) (eqn (8)) and Fe(0)/Fe(III) (eqn (7)); and another anodic peak at around −0.47 V (E_{pa2}), attributed to the oxidation of Fe(II)/Fe(III). With further cycling for more cycles at 50 mV s^{-1}, the cathodic peaks and anodic peaks don't shift toward a more negative potential or move to a more positive potential. A similar behaviour was apparent for the cycling at sweep rates of 100–300 mV s^{-1}, moreover, the location of the cathodic peak potentials and anodic peak potentials is nearly constant with increase of the sweep rate. This suggests that the reversible deposition–dissolution of iron occurs.

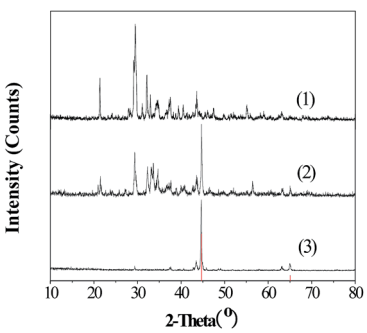

Fig. 6 XRD patterns (1) of the electrolyte after charging, (2) of products on the steel electrode after charging, and (3) of products separated with a magnetic stirrer after washing with water to remove the electrolyte. Red vertical lines: XRD library pure iron spectra, PDF: 06-0696.

Morphology and ORR characteristics of the fin air electrode configuration

The performance of the metal–air battery is also strongly dependent on the efficacy of the air electrode, namely the rate of the oxygen reduction reaction. In order to improve the cell performance, we changed the air electrode structure and maximized the surface area of the air electrode to increase the reaction rate. Thus a fin type air electrode, *in lieu* of the previous cylindrical air electrode, was designed and employed. As shown in Fig. 7, the fin part for the ORR is oriented towards the air side and the planar side faces the electrolyte used for the OER. The fin air electrode was extracted from the electrolyte subsequent to charge–discharge cycling, and washed with water to remove

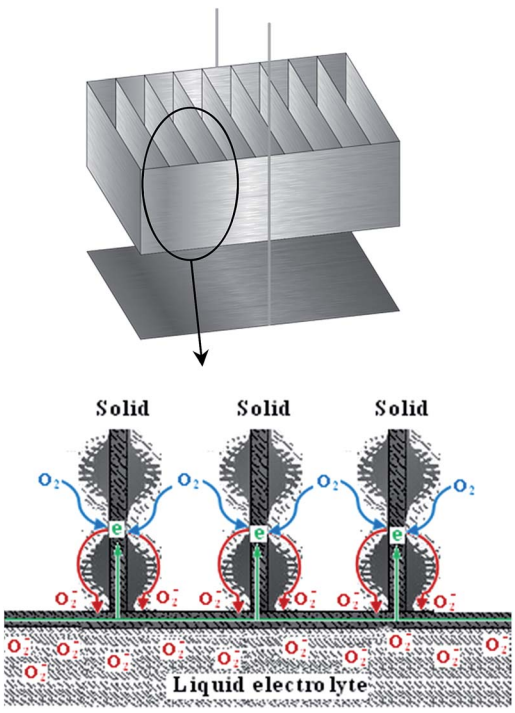

Fig. 7 Top: Schematic drawing of the electrode configuration, upper: the fin type air electrode (1 cm height), and lower: the steel electrode (2 cm ×2.5 cm). Bottom: Schematic drawing of the triple-phase interface and ORR characteristics of the fin type air electrode.

the electrolyte. The structure and morphology were investigated by XRD and FE-SEM.

Compared to the fresh air electrode, the fin type air electrode has developed a black coating on the surface after charge–discharge. The XRD analysis of the black electrode exhibits not only three 2-theta peaks of nickel but also five 2-theta peaks of nickel oxide at 37.24, 43.26, 62.84, 75.37 and 79.36° and also peaks of lithium nickel oxide at $2\theta = 18.45$, 37.26, 37.4, 44.74, and 64.14° (Fig. 8). The intense and sharp diffraction peaks suggest that the obtained nickel oxides and lithium nickel oxides were well crystallized. We suggest that Ni is oxidized *in situ* to nickel oxide and lithium nickel oxide inside the cell during the charge–discharge of iron molten air batteries. The microstructural and morphological properties of the air electrode were further explored by FE-SEM (Fig. 9). SEM images reveal that NiO particles pack densely on the surface layer (Fig. 9a and b). The smaller particles are mostly imbedded inside the void space of the larger particles (Fig. 9c and d). The particle sizes of NiO are found to range between 100 and 300 nm. Lithium nickel oxide itself has excellent catalytic activity for the OER/ORR at a high temperature.[26] The air electrode also doesn't require any conductive substrates such as carbon materials to help electron transport from the current collector to the surface of

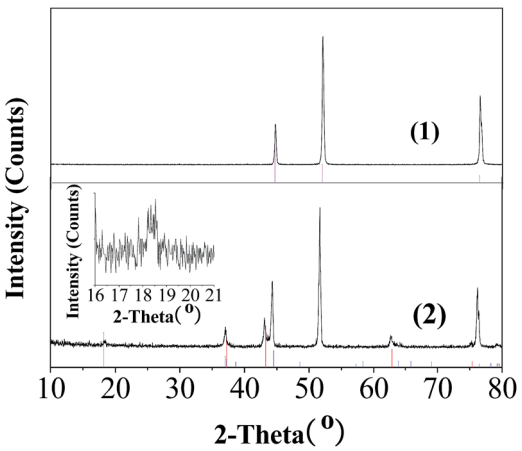

Fig. 8 XRD analysis of the fin type air electrode. (1) XRD pattern of the fresh air electrode. Pink vertical lines: XRD library pure nickel spectra, PDF: 70-1849. (2) XRD and high resolution XRD (inset) patterns of the air electrode after the charge–discharge cycle. Red vertical lines: XRD library nickel oxide spectra, PDF: 78-0423; blue vertical lines: XRD library lithium nickel oxide, $(Li_{0.05}Ni_{0.05})(NiO_2)$, spectra, PDF: 85-1987.

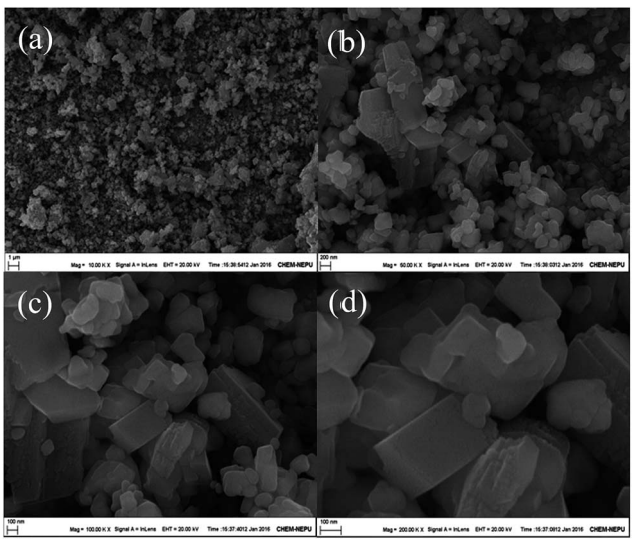

Fig. 9 SEM images of the fin type air electrode fins after 450 cycles. At (a) 10 000×, (b) 50 000×, (c) 100 000×, and (d) 200 000×.

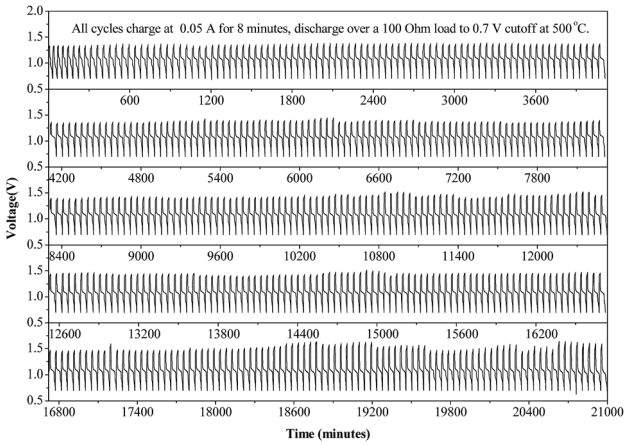

Fig. 10 Cycled charge–discharge behavior of the iron molten air battery with a 56.5 mol% $Li_{0.87}Na_{0.63}K_{0.50}CO_3$ eutectic–43.5 mol% LiOH electrolyte containing 0.5 m Fe_2O_3 and 3 m NaOH at 500 °C. Cycle charges at 0.05 A for 8 minutes and discharges over a 100 Ω load to a 0.7 V cutoff.

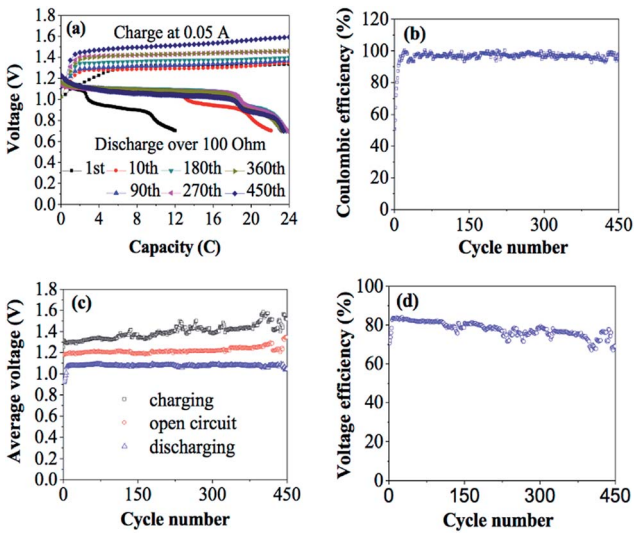

Fig. 11 Cycle performance of the iron molten air battery with a 56.5 mol% $Li_{0.87}Na_{0.63}K_{0.50}CO_3$ eutectic–43.5 mol% LiOH electrolyte containing 0.5 m Fe_2O_3 and 3 m NaOH at 500 °C. (a) Voltage profiles for 1st, 10th, 90th, 180th, 270th, 360th and 450th cycles. (b) Coulombic efficiency. (c) Average voltage of charging, open circuit and discharging. (d) Voltage efficiency. Cycle charges at 0.05 A for 8 minutes and discharges over a 100 Ω load to a 0.7 V cutoff.

nickel oxide and lithium nickel oxide particles because nickel oxide and lithium nickel oxide, differing from other metal oxide OER/ORR catalysts such as MnO_2 and Co_2O_3, have adequate electronic conductivity which approaches that of metal conductivity. Moreover, nanostructured materials for rechargeable batteries provide enhanced kinetics because of their large surface areas, short diffusion lengths, and fast diffusion rates.[32]

We found that the liquid electrolytes spread over the fin air electrode surface due to wetting when the electrode interacts with the electrolyte. Compared to conventional porous air electrodes used in metal–air batteries, no air electrode flooding with the electrolyte occurs in the fin air electrode. Further, the nano-NiO particles on the fin are covered and stay relatively "wet" by a thin liquid electrolyte film, being capable of diffusing oxygen to conform a triple-phase interface of gas–liquid–solid (oxygen, electrolyte, and catalysts). As illustrated in Fig. 7, the reactant gases (oxygen) can access easily the reaction zone through relatively open gas channels and the liquid film, at the same time, electrons also gain access to the surface of the NiO catalyst in the electrodes. Generally, the high rate of the oxygen reduction reaction is reached when approaching the triple-phase interface during discharge. At the same time, the product oxygen ions must be able to move back from the catalyst surface to the electrolyte.

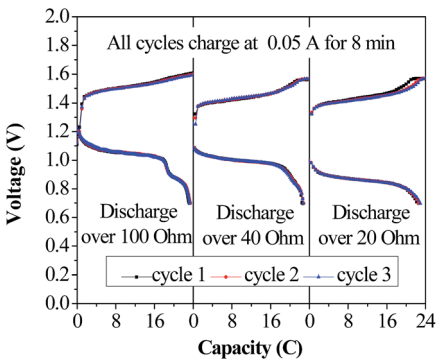

Fig. 12 The rate capacities of the iron molten air battery with a 56.5 mol% $Li_{0.87}Na_{0.63}K_{0.50}CO_3$ eutectic–43.5 mol% LiOH electrolyte containing 0.5 m Fe_2O_3 and 3 m NaOH at 500 °C. Cycle charges at 0.05 A for 8 minutes and discharges over loads of 100, 40 and 20 Ω (each load for three cycles) to a 0.7 V cutoff.

Cycling characteristics

To investigate the cycle performances of the cell, the iron molten air battery with the fin air electrode was tested with a repeated cycle of charging at 0.05 A and discharging over a 100 Ω load to a 0.7 V cutoff at 500 °C. As shown in Fig. 10, the battery cycled stably for 450 cycles in molten 56.5 mol% $Li_{0.87}Na_{0.63}K_{0.50}CO_3$ eutectic–43.5 mol% LiOH with 0.5 m Fe_2O_3 and 3 m NaOH in air. As seen in Fig. 11a and b, the battery exhibits a discharge voltage plateau at about 0.9 V and a coulombic efficiency of 50.6% in the first cycle because formation of the NiO catalyst layer is only just beginning on the air electrode. Thereafter, the discharge voltage plateau and coulombic efficiency increase quickly, and reach 1.07 V and 91.9% in the 10th cycle, respectively, indicating that the NiO catalyst layer on the air electrode has formed completely within the first ten cycles, a start-up stage. After the start-up, the battery exhibits an excellent long term stability, and no evident coulombic efficiency fading was observed for 450 cycles. The coulombic efficiencies for majority of cycles almost approached 100%. As shown in Fig. 11a two discharge voltage plateaus are present in all cycles. The upper voltage plateau discharge can be attributed to the discharge of Fe^0 to Fe^{2+} and Fe^0 to Fe^{3+}, and the lower can be ascribed to the discharge of Fe^{2+} to Fe^{3+} as previously observed by voltammetry in Fig. 4. As seen from Fig. 11c and d, the average open circuit voltage was around ~1.18 V, and the average discharge potential was about ~1.08 V for majority of cycles. However, the average charge potential increased slowly with battery cycling due to polarization, but was under 1.58 V of the highest average charge potential. The voltage efficiency reached the highest, 83.6%, in the sixteenth cycle, then decreased slowly with battery cycling, and the lowest voltage efficiency was 66.8% in the 403rd cycle. A future paper will seek to understand the reason for the charging polarization becoming severe with battery cycling, and find a solution. No obvious corrosion was visible on the air electrode after 450 cycles (350 hours) at 500 °C.

Rate performances

In order to study the rate capability of the battery, after long cycles, the operating mode is switched: charge at 0.05 A for 8 minutes, then discharge over loads of 100, 40 and 20 Ω (each

Table 1 The detailed rate capacities of the iron molten air battery with a 56.5 mol% $Li_{0.87}Na_{0.63}K_{0.50}CO_3$ eutectic–43.5 mol% LiOH electrolyte containing 0.5 m Fe_2O_3 and 3 m NaOH at 500 °C. The indicated discharge current density is normalized by the 5 cm^2 anode surface

Ω_{load}	Cycle	Average discharge current (mA)	Discharge current density (mA cm^{-2})	Rate (C)	Coulombic efficiency (%)	Voltage efficiency (%)	Average coulombic efficiency (%)	Average voltage efficiency (%)
100	Cycle 1	10.4	2.1	1.6	96.8	68.7	97.4	68.9
	Cycle 2	10.5	2.1	1.6	97.9	69.1		
	Cycle 3	10.4	2.1	1.6	97.5	68.9		
40	Cycle 1	24.8	5.0	3.7	94.5	69.2	94.9	68.9
	Cycle 2	24.8	5.0	3.7	95.1	68.7		
	Cycle 3	24.8	5.0	3.7	95	68.7		
20	Cycle 1	43	8.6	6.4	94.6	59.8	95.1	59.9
	Cycle 2	43	8.6	6.4	94.7	60.1		
	Cycle 3	43	8.6	6.4	96.2	59.9		

load for three cycles) to a 0.7 V cutoff at 500 °C, respectively. The discharge capacities at different loads are shown in Fig. 12 (the detailed rate capabilities are given in Table 1). As shown in Fig. 12, the discharge voltage plateaus decrease with the decrease of the discharge load, since the electrochemical polarization becomes much more significant at higher discharge current densities. The battery exhibits a high coulombic efficiency, as shown in Table 1, the coulombic efficiencies are 97.4, 94.9 and 95.1%, respectively, when discharging at a low rate of 1.6C as well as at high rates of 3.7 and 6.4C. This demonstrates the excellent rate performance of the iron molten air battery.

Conclusions

We demonstrate an iron molten air battery utilizing a nickel fin air electrode configuration and a $Li_{0.87}Na_{0.63}K_{0.50}CO_3$ eutectic electrolyte with added LiOH. Addition of LiOH to the $Li_{0.87}Na_{0.63}K_{0.50}CO_3$ eutectic decreases the discharge polarization. Cyclic voltammetry studies indicated that deposition–dissolution of iron is reversible in the electrolyte. FE-SEM and XRD results indicated that nanostructured nickel oxide and lithium nickel oxide particles were formed *in situ* on the air electrode. Oxygen maintains facile access to the reaction zone *via* the nickel fin air electrode configuration without flooding by the electrolyte. The battery showed an excellent rate performance and a stable cycling performance through 450 cycles with nearly 100% coulombic efficiency and an average discharge potential of ~1.08 V when charged at a constant current of 0.05 A and discharged over a constant 100 Ω load to a 0.7 V cutoff at 500 °C.

Acknowledgements

This work was supported by the National Natural Science Foundation of China (Grant No. 21473028) and the Postdoctoral Scientific Research Development Fund of Heilongjiang Province, China (Grant No. LBH-Q14029). We appreciate the assistance of the Analysis Test Center of the College of Chemistry and Chemical Engineering, Northeast Petroleum University in collecting XRD and FE-SEM data. Licht is grateful to the US NSF (Award 1505830) for partial support of this study.

Notes and references

1 N. Zhao, C. Li and X. X. Guo, *Phys. Chem. Chem. Phys.*, 2014, **16**, 15646–15652.
2 Z. L. Wang, D. Xu, J. J. Xu and X. B. Zhang, *Chem. Soc. Rev.*, 2014, **43**, 7746–7786.
3 F. Cheng and J. Chen, *Chem. Soc. Rev.*, 2012, **41**, 2172–2192.
4 I. Hadjipaschalis, A. Poullikkas and V. Efthimiou, *Renewable Sustainable Energy Rev.*, 2009, **13**, 1513–1522.
5 https://en.wikipedia.org/wiki/Iron, access September 24, 2016.
6 S. Licht, B. C. Cui, J. Stuart, B. H. Wang and J. Lau, *Energy Environ. Sci.*, 2013, **6**, 3646–3657.
7 S. R. Narayanan, G. K. Surya Prakash, A. Manohar, B. Yang, S. Malkhandi and A. Kindler, *Solid State Ionics*, 2012, **216**, 105–109.
8 R. D. McKerracher, C. P. de Leon, R. G. A. Wills, A. A. Shah and F. C. Walsh, *ChemPlusChem*, 2015, **80**, 323–335.
9 B. T. Hang, H. Hayashi, S.-H. Yoon, S. Okada and J. Yamaki, *J. Power Sources*, 2008, **178**, 393–401.
10 B. T. Hang, D. H. Thang and E. Kobayashi, *J. Electroanal. Chem.*, 2013, **704**, 145–152.
11 T. Kim, Y. Ohata, J. Kim, C. K. Rhee, J. Miyawaki and S.-H. Yoon, *Carbon*, 2014, **80**, 698–707.
12 A. K. Manohar, S. Malkhandi, B. Yang, C. Yang, G. K. S. Prakash and S. R. Narayanan, *J. Electrochem. Soc.*, 2012, **159**, A1209–A1214.
13 A. K. Manohar, C. Yang, S. Malkhandi, G. K. S. Prakash and S. R. Narayanan, *J. Electrochem. Soc.*, 2013, **160**, A2078–A2084.
14 H. Kitamura, L. Zhao, B. T. Hang, S. Okada and J. Yamaki, *J. Electrochem. Soc.*, 2012, **159**, A720–A724.
15 B. T. Hang, D. H. Thang, N. T. Nga, P. T. L. Minh and E. Kobayashi, *J. Electrochem. Soc.*, 2013, **160**, A1442–A1445.
16 A. Ito, L. Zhao, S. Okada and J. Yamaki, *J. Power Sources*, 2011, **196**, 8154–8159.
17 A. S. Rajan, S. Sampath and A. K. Shukla, *Energy Environ. Sci.*, 2014, **7**, 1110–1116.
18 T. Tsuneishi, H. Sakamoto, K. Hayashi, G. Kawamurac, H. Muto and A. Matsuda, *Journal of Asian Ceramic Societies*, 2014, **2**, 165–168.
19 N. S. Xu, X. Li, X. Zhao, J. B. Goodenough and K. Huang, *Energy Environ. Sci.*, 2011, **4**, 4942–4946.
20 A. Inoishi, S. Ida, S. Uratani, T. Okano and T. Ishihara, *Phys. Chem. Chem. Phys.*, 2012, **14**, 12818–12822.
21 A. Inoishi, T. Sakai, Y. W. Ju, S. Ida and T. Ishihara, *J. Power Sources*, 2014, **262**, 310–315.
22 B. C. Cui and S. Licht, *J. Mater. Chem. A*, 2014, **2**, 10577–10580.
23 S. Z. Liu, X. Li, B. C. Cui, X. J. Liu, Y. L. Hao, Q. Guo, P. Q. Xu and S. Licht, *J. Mater. Chem. A*, 2015, **3**, 21039–21043.
24 S. Z. Liu, W. Han, B. C. Cui, X. J. Liu, F. L. Zhao, J. Stuart and S. Licht, *J. Power Sources*, 2017, **342**, 435–441.
25 EG&G Technical Services, Inc, *Fuel cell handbook*, Morgantown, West Virginia, USA, 7th edn, 2004.
26 K. D. Kreuer, *Fuel Cells*, Springer Science+Business Media, New York, 2013.
27 D. J. Fray, *JOM*, 2001, **53**, 27–31.
28 H. Wu, D. Ji, L. Li, D. Yuan, Y. Zhu, B. Wang, Z. Zhang and S. Licht, *Adv. Mater. Technol.*, 2016, **1**, 1600092.
29 S. Licht, *J. Phys. Chem. C*, 2009, **113**, 16283–16292.
30 Thermochemical data are available online at U.S. National Institute of Standards and Technology ChemWeb: http://webbook.nist.gov/chemistry/form-ser.html.
31 Glenn Research Center, National Aeronautics and Space Administration (NASA), ThermoBuild access to NASA Glenn thermodynamic CEA database (2006); data available at http://www.grc.nasa.gov/WWW/CEAWeb/ceaThermoBuild.htm.
32 H. Kim, G. Jeong, Y.-U. Kim, J.-H. Kim, C.-M. Park and H.-J. Sohn, *Chem. Soc. Rev.*, 2013, **42**, 9011–9034.